

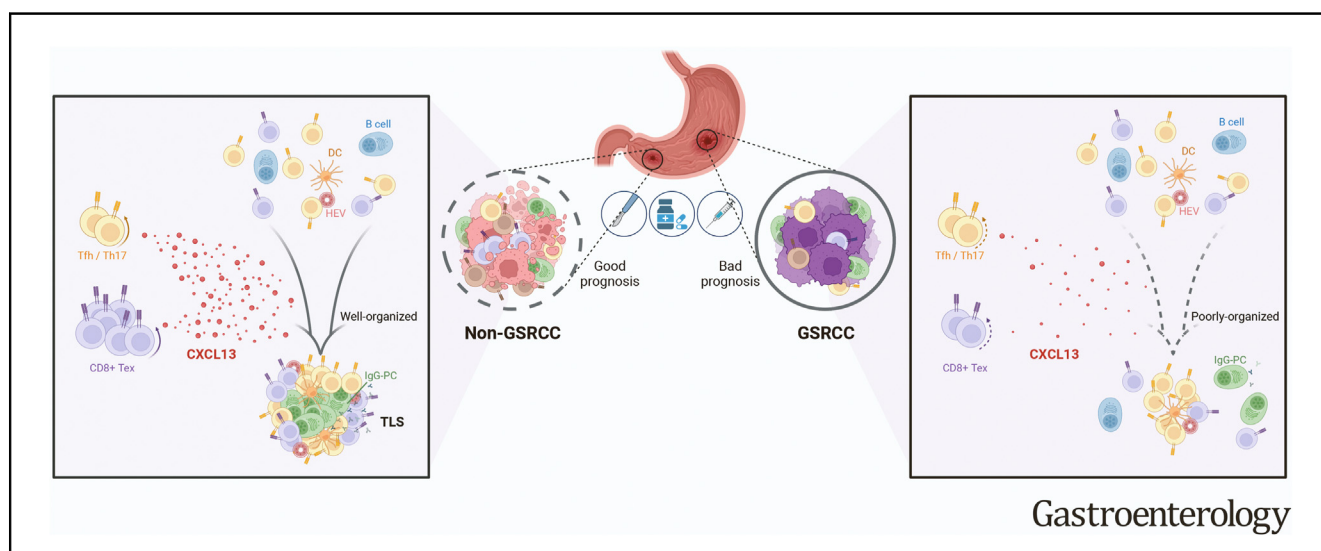
## GI CANCER

## Single-Cell Profiling of Tumor Immune Microenvironment Reveals Immune Irresponsiveness in Gastric Signet-Ring Cell Carcinoma



Jing Chen,<sup>1,\*</sup> Kuai Liu,<sup>2,3,4,\*</sup> Yikai Luo,<sup>5,6,\*</sup> Muxing Kang,<sup>1</sup> Jun Wang,<sup>1</sup> Guofeng Chen,<sup>1</sup> Jia Qi,<sup>1</sup> Wenxuan Wu,<sup>1</sup> Beidi Wang,<sup>1</sup> Yaxuan Han,<sup>1</sup> Le Shi,<sup>1</sup> Kefan Wang,<sup>1</sup> Xiaying Han,<sup>1</sup> Xiaojing Ma,<sup>7</sup> Wei Liu,<sup>6</sup> Yuan Ding,<sup>8</sup> Liangjing Wang,<sup>9,4</sup> Han Liang,<sup>6,10,5</sup> Lie Wang,<sup>2,3,4</sup> and Jian Chen<sup>1,4</sup>

<sup>1</sup>Department of Gastrointestinal Surgery, The Second Affiliated Hospital, Zhejiang University School of Medicine, Hangzhou, China; <sup>2</sup>Institute of Immunology and Bone Marrow Transplantation Center, The First Affiliated Hospital, Zhejiang University School of Medicine, Hangzhou, China; <sup>3</sup>Liangzhu Laboratory, Zhejiang University Medical Center, Hangzhou, China; <sup>4</sup>Cancer Center, Zhejiang University, Hangzhou, China; <sup>5</sup>Graduate Program in Quantitative and Computational Biosciences, Baylor College of Medicine, Houston, Texas; <sup>6</sup>Department of Bioinformatics and Computational Biology, The University of Texas MD Anderson Cancer Center, Houston, Texas; <sup>7</sup>Department of Pathology, The Second Affiliated Hospital, Zhejiang University School of Medicine, Hangzhou, China; <sup>8</sup>Department of Surgery, The Second Affiliated Hospital, Zhejiang University School of Medicine, Hangzhou, China; <sup>9</sup>Department of Gastroenterology, The Second Affiliated Hospital, Zhejiang University School of Medicine, Hangzhou, China; and <sup>10</sup>Department of Systems Biology, The University of Texas MD Anderson Cancer Center, Houston, Texas



**BACKGROUND & AIMS:** Gastric cancer (GC) is a major cancer type characterized by high heterogeneity in both tumor cells and the tumor immune microenvironment (TIME). One intractable GC subtype is gastric signet-ring cell carcinoma (GSRCC), which is associated with poor prognosis. However, it remains unclear what the GSRCC TIME characteristics are and how these characteristics may contribute to clinical outcomes. **METHODS:** We enrolled 32 patients with advanced GC of diverse subtypes and profiled their TIME using an immune-targeted single-cell profiling strategy, including (1) immune-targeted single-cell RNA sequencing ( $n = 20$  patients) and (2) protein expression profiling by a targeted antibody panel for mass cytometry ( $n = 12$  patients). We also generated matched V(D)J (variable, diversity, and joining gene segments) sequencing of T and B cells along CD45<sup>+</sup> immunocytes.

**RESULTS:** We found that compared to non-GSRCC, the GSRCC TIME appears to be quiescent, where both CD4<sup>+</sup> and CD8<sup>+</sup> T cells are difficult to be mobilized, which further impairs the proper functions of B cells. CXCL13, mainly produced by follicular helper T cells, T helper type 17, and exhausted CD8<sup>+</sup> T cells, is a central coordinator of this transformation. We show that CXCL13 expression can predict the response to immune checkpoint blockade in GC patients, which may be related to its effects on tertiary lymphoid structures. **CONCLUSIONS:** Our study provides a comprehensive molecular portrait of immune cell compositions and cell states in advanced GC patients, highlighting adaptive immune irresponsiveness in GSRCC and a mediator role of CXCL13 in TIME. Our targeted single-cell transcriptomic and proteomic profiling represents a powerful approach for TIME-oriented translational research.

**Keywords:** Gastric Cancer; T-Cell State; CXCL13; Immune Checkpoint Blockade.

Gastric cancer (GC) is one of the most malignant diseases, ranking fifth for incidence and fourth for mortality worldwide,<sup>1</sup> with remarkable heterogeneity. The main classification systems in clinical practice include Lauren's classification (intestinal and diffuse) and the World Health Organization classification (papillary, tubular, mucinous, and poorly cohesive).<sup>2,3</sup> Gastric signet ring cell carcinoma (GSRCC) is a special subtype of diffuse GC in Lauren's system or poorly cohesive GC in the World Health Organization system and is characterized by prominent mucin in the cytoplasm and eccentric nucleus. GSRCC is poorly differentiated, associated with a higher ratio of metastasis and recurrence, and has been recognized as an independent predictor of poor prognosis.<sup>4</sup>

Clinical management of advanced GC remains conventional and limited. Radical surgery is the only curative option, whereas chemotherapy can improve the outcome of resectable tumors or help those diagnosed with disease that is too advanced for curative resection. Targeted drugs like trastuzumab and pertuzumab have been applied for HER-2-positive GC patients.<sup>5</sup> Immune checkpoint blockade (ICB) therapy has been evaluated in clinical trials, but the results are far from heartening, with low response rates and limited survival improvement.<sup>6-8</sup> Furthermore, GC patients are treated with almost the same strategy regardless of their distinct tumor subtypes, leading to varied clinical outcomes, such as poor responsiveness of chemo- and immunotherapies for GSRCC patients.

Multomics analyses have captured the intrinsic characteristics of tumor cells from primary and/or metastatic sites.<sup>9,10</sup> However, the tumor immune microenvironment (TIME), a key factor that affects carcinogenesis, progression, and prognosis,<sup>11</sup> remains poorly characterized. Several studies have characterized the immune components in GC using single-cell analysis without any hierarchy, potentially overlooking the uniqueness of certain GC subtypes.<sup>12,13</sup> Presumably, TIME heterogeneity is largely derived from tumor heterogeneity and, in turn, influences cancer cell behaviors and clinical outcome.<sup>14,15</sup> Therefore, we decided to investigate whether GSRCC has a unique scenario of the TIME and how its TIME characteristics may contribute to a poor prognosis.

## Materials and Methods

Details about experimental procedures and data analysis are provided in the [Supplementary Methods](#).

## Results

### *An Immune-Targeted Single-Cell RNA-Sequencing Platform Accurately Captures the Gastric Cancer Tumor Immune Microenvironment*

To decipher the TIME heterogeneity of GSRCC vs non-GSRCC, we enrolled 32 patients with newly diagnosed

## WHAT YOU NEED TO KNOW

### BACKGROUND AND CONTEXT

Gastric signet-ring cell carcinoma (GSRCC) is a rare pathologic type of gastric cancer (GC) that bears high invasiveness, metastatic capabilities, and poor prognosis. A high-resolution cellular and molecular profile of its tumor immune microenvironment (TIME) has not been available.

### NEW FINDINGS

The TIME of advanced GSRCC is enriched for immunosuppressive factors, including the loss of CXCL13-expressing terminally differentiated CD8<sup>+</sup> T cells and the decline of clonal crosstalk among populations of T and B cells. Consistent with weakened formation of tertiary lymphoid structures in GSRCC, the expression level of CXCL13 shows the most robust predictive power of a favorable tumor response to anti-PD1 treatment in GC patients.

### LIMITATIONS

This study is largely observational, with a relatively limited sample size. Functional assays are needed to further characterize the role of CXCL13 in coordinating the immunosuppression of GSRCC.

### CLINICAL RESEARCH RELEVANCE

This study highlights the importance of CXCL13-producing exhausted CD8<sup>+</sup> T cells in promoting antitumor response. For non-GSRCC patients, it may be feasible for them to take conventional treatment, including chemotherapy and/or immune checkpoint blockade, whereas for GSRCC patients, it may be crucial to improve the CXCL13-producing ability of exhausted CD8<sup>+</sup> T cells to reverse the refractory condition.


### BASIC RESEARCH RELEVANCE

This study provides an adaptive immune atlas of GSRCC at the single-cell level for the first time to our knowledge, reveals the roles of specific T- and B-cell states in mediating an irresponsive TIME, and nominates CXCL13 as a central coordinator of GC TIME activation through its direct effect on tertiary lymphoid structure maturation.

advanced GC, including 20 in the single-cell RNA sequencing (scRNA-seq) cohort and 12 in the cytometry by time of flight (CyTOF) cohort ([Supplementary Tables 1-3](#)). All tumors of

\* Authors share co-first authorship.

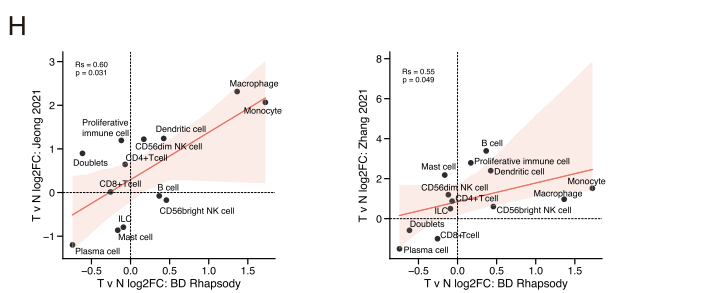
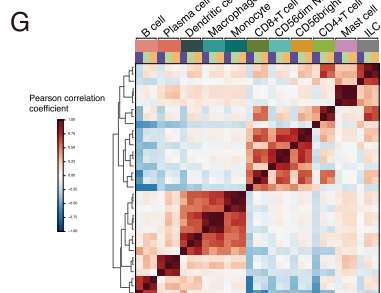
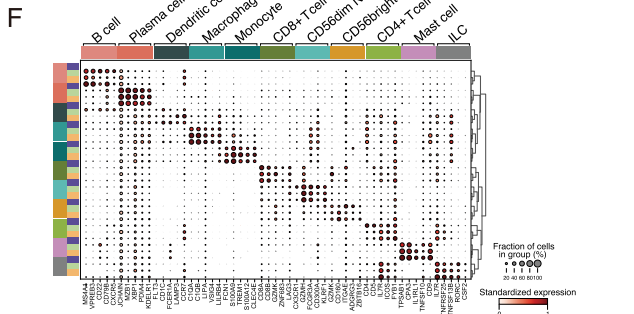
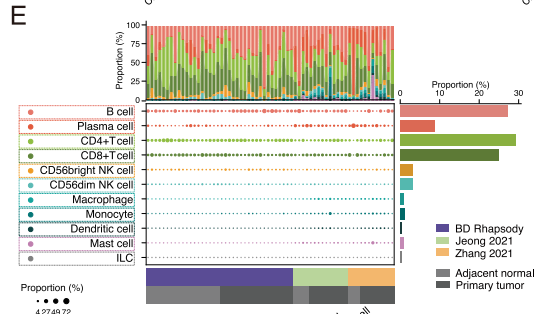
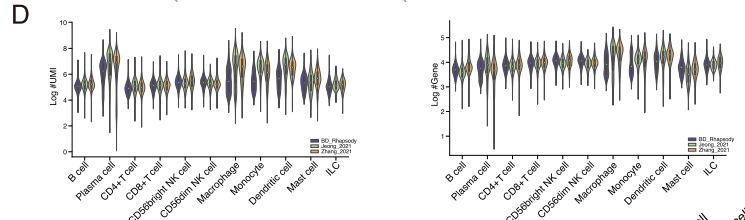
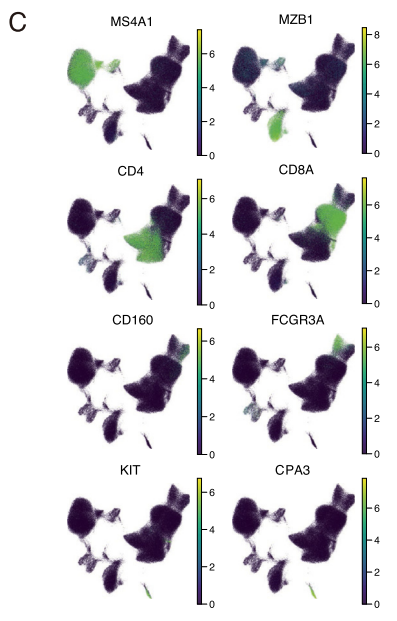
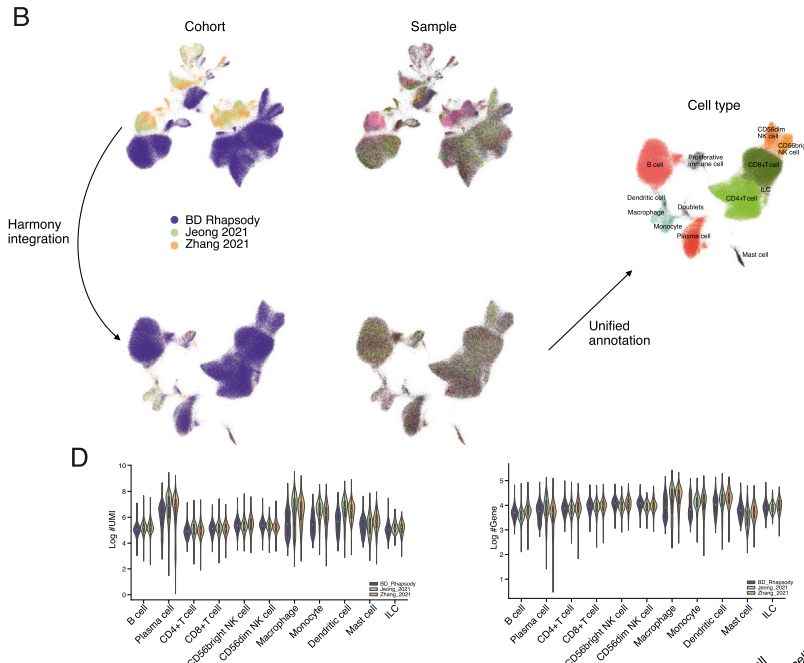
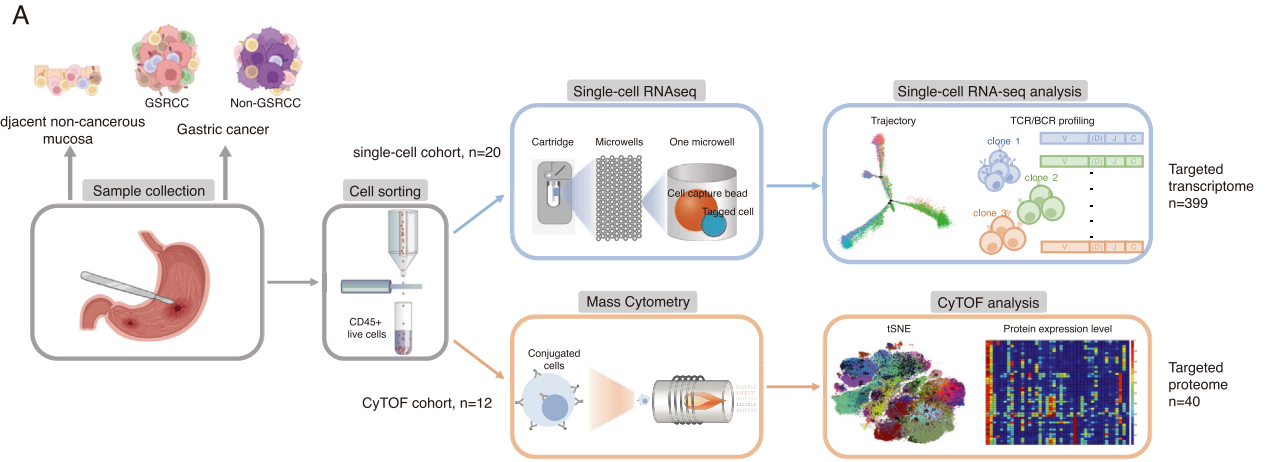
**Abbreviations used in this paper:** BCR, B-cell receptor; CyTOF, cytometry by time of flight; DEG, differentially expressed gene; GC, gastric cancer; GSRCC, gastric signet-ring cell carcinoma; ICB, immune checkpoint blockade; MAIT, mucosal-associated invariant T cell; PC, plasma cell; scRNA-seq, single-cell RNA sequencing; SHM, somatic hypermutation; TCR, T-cell receptor; T<sub>eff</sub>, effector T cell; T<sub>ex</sub>, exhausted T cell; T<sub>fh</sub>, follicular helper T cell; T<sub>h</sub>, T helper; TIME, tumor immune microenvironment; TLS, tertiary lymphoid structure; T<sub>n</sub>, naive T cell; T<sub>reg</sub>, regulatory T cell; T<sub>rm</sub>, resident memory T cell; UMAP, uniform manifold approximation and projection.

 Most current article

© 2023 The Author(s). Published by Elsevier Inc. on behalf of the AGA Institute. This is an open access article under the CC BY-NC-ND license (<http://creativecommons.org/licenses/by-nc-nd/4.0/>).

0016-5085

<https://doi.org/10.1053/j.gastro.2023.03.008>



advanced stages were histopathologically classified as GSRCC or non-GSRCC and were naive to chemotherapy or radiotherapy before surgery (Supplementary Figure 1A). Fresh tissues from these patients collected during surgery were immediately dissociated into single cells, followed by fluorescence-activated cell sorting for live CD45<sup>+</sup> immunocytes (>99% cell purity) (Supplementary Figure 1B). The acquired cells were later profiled by immune-targeted scRNA-seq with matched T-cell receptor (TCR)/B-cell receptor (BCR) sequencing or T--targeted CyTOF profiling (Figure 1A).

To validate our targeted scRNA-seq platform, we first performed multifaceted analyses on an integrated GC TIME atlas that combined our data with 2 published datasets where cells were sequenced based on the 10x Genomics whole-transcriptome sequencing scheme<sup>9,15</sup> (Supplementary Figure 1C). With computational integration by Harmony<sup>16</sup> (Figure 1B and Supplementary Figure 1D and E), we confirmed that both platforms gauged a common identity manifold established by the core gene expression programs specific to each immune cell population. We then annotated this unified GC TIME atlas according to the expression of canonical gene markers in major immune populations (Figure 1C). Sequencing depth and transcriptome complexity were comparable between the targeted sequencing platform and the 10x platform (Figure 1D). Across the platforms, cells from each population existed in a consistent proportion (Figure 1E and Supplementary Figure 1F), showed highly similar marker expressions (Figure 1C and F), and were grouped by a shared transcription landscape (Figure 1G). Importantly, tumor-induced alterations in TIME composition demonstrated by all 3 datasets were in good concordance (Figure 1H). These results demonstrate that the immune-targeted scRNA-seq platform can serve as an effective alternative in dissecting GC TIME at a single-cell resolution.

### Distinct T-Cell Subset Compositions Between Gastric Signet-Ring Cell Carcinoma and Non-Gastric Signet-Ring Cell Carcinoma

Globally, adaptive immunocytes, including T and B cells, accounted for >75% of our immune-targeted transcriptome profiles (Supplementary Figure 2A and B). We next sub-clustered a total of 53,768 T cells, spanning 20 donors, into 8 CD4<sup>+</sup> and 5 CD8<sup>+</sup> subsets in the scRNA-seq cohort

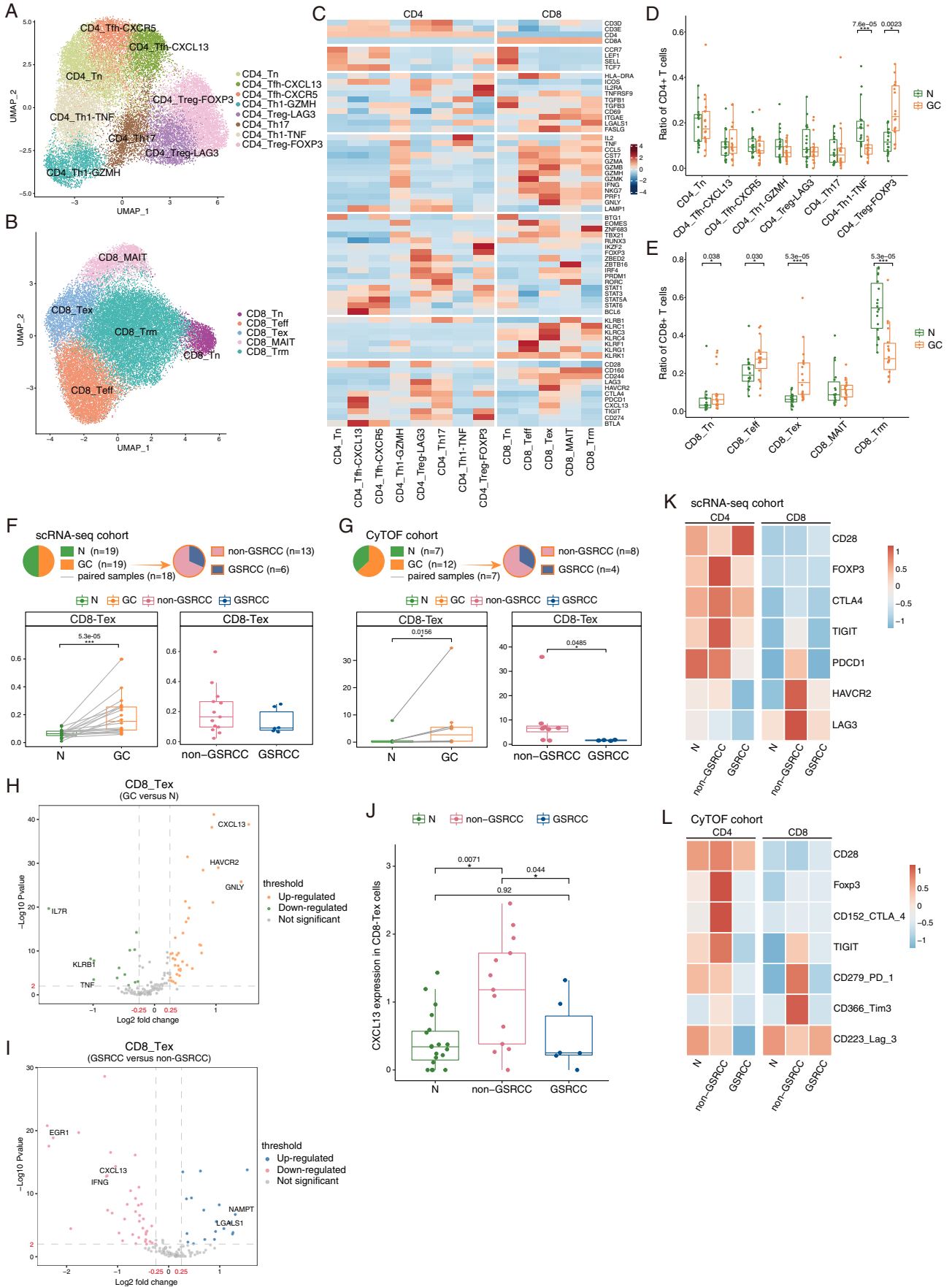
(Figure 2A–C and Supplementary Figure 2C and D). Expression signatures revealed T-cell subsets both well described and newly annotated, including typical CCR7<sup>+</sup> naive CD4<sup>+</sup> and CD8<sup>+</sup> T cells (Tn), follicular helper T cells (Tfh), T helper (Th) type 1, Th17, regulatory T cells (Treg), effector CD8<sup>+</sup> T cells (CD8-Teff), HAVCR2<sup>+</sup> (encoding TIM-3) exhausted CD8<sup>+</sup> T cells (CD8-Tex), NCR3<sup>+</sup> mucosal-associated invariant T cells (CD8-MAIT), and ZNF683-characterized tissue-resident memory CD8<sup>+</sup> T cells (CD8-Trm). We further divided the sister subsets of Th1 and Tfh into pre-effector (Th1-TNF, Tfh-CXCR5) and terminal effector populations (Th1-GZMH, Tfh-CXCL13).<sup>17</sup> In contrast, the 2 Treg subsets (Treg-FOXP3 and Treg-LAG3) did not match the canonical classification of natural Treg vs induced Treg,<sup>18</sup> indicating a unique separation of Treg functional states in the GC TIME. Specifically, Treg-FOXP3 presented more activation features (IL2RA, IKZF2),<sup>19</sup> whereas Treg-LAG3 expressed a higher level of inhibitory receptors (LAG3, HAVCR2, PDCD1, TIGIT) (Figure 2C). We next assigned T-cell targeted subsets in the CyTOF cohort and obtained similar T-cell components in CD3<sup>+</sup> T-cell-targeted CyTOF profiles, among which diverse Treg subsets exhibited the same features (Supplementary Figure 2E and F).

Compared to adjacent noncancerous mucosa, there was a significantly lower ratio of Th1 and CD8-Trm cells but a higher proportion of Treg-FOXP3 and CD8-Tex cells in GC (Figure 2D–F and Supplementary Figure 2J). The augmentation observed in Treg-FOXP3 but not in Treg-LAG3 suggested the former population as tumor-induced Treg. The emergence and accumulation of CD8-Tex cells have been accepted as the main obstacle to optimal tumor control.<sup>20</sup> In the CyTOF cohort, we observed a similar profile of significantly increased CD8-Tex and Treg-FOXP3 in GC (Figure 2G and Supplementary Figure 2J).

Intriguingly, we noticed opposite alterations of Treg-FOXP3 and CD8-Tex in a comparison between GSRCC and non-GSRCC (Supplementary Figure 2G and H). Validated by the CyTOF results, the decrease of CD8-Tex in GSRCC conflicted with the anticipation that the enrichment of this dysfunctional population would contribute to the worse prognosis of GSRCC (Figure 2G). We, therefore, sought to reconcile this conflict by examining the cancer-induced dynamic of specific molecular signatures of CD8-Tex. Indeed, the tumor association of CD8-Tex was supported by antigen stimulation-derived GNLY and HAVCR2 that was greatly up-

**Figure 1.** Study design and the validation of the immune-targeted scRNA-seq platform. (A) Schematic diagram of the study design. Single live immunocytes (CD45<sup>+</sup>) obtained from GC and adjacent noncancerous tissues were applied to scRNA-seq (n = 20) or CyTOF (n = 12) profiling and analysis. (B) UMAP plot of CD45<sup>+</sup> cells merged from our data and 2 published GC datasets, preintegration (top), postintegration (bottom), or with major immune populations annotated (right). (C) UMAP plot of integrated immune cell atlas colored by the expression levels of canonical gene markers. (D) Violin plots showing the distributions of per-cell UMI count (left) and gene count (right) across immune populations in different datasets. (E) Heatmap showing the relative proportions of immune populations in individual samples across datasets and disease conditions. (F) Heatmap showing the magnitude and sparsity of marker gene expressions across immune populations in different datasets. (G) Heatmap showing the interpopulation gene expression correlation across datasets. (H) Scatter plots showing the correlations between tumor vs nontumor population abundance changes in different datasets. FC, fold change; ILC, innate lymphoid cells; N, nontumor; NK, natural killer; R<sub>s</sub>, Spearman correlation coefficient; T, tumor; UMAP, uniform manifold approximation and projection; UMI, unique molecular identifier.





regulated in GC. Furthermore, the chemoattractant-encoding gene CXCL13 was also greatly up-regulated in cancer-specific CD8-Tex (Figure 2H). In contrast, this CXCL13-mediated regulatory effect of CD8-Tex was substantially down-regulated in GSRCC, together with other effector and activation features (IFNG, EGR1) (Figure 2I and J). Moreover, a negative regulator to the effectiveness of CD8<sup>+</sup> T cells, LGALS1 was up-regulated in GSRCC CD8-Tex<sup>21</sup> (Figure 2I). Collectively, these observations on the functional state shift of CD8-Tex suggest a model where the less cytotoxic population acquired the ability to produce CXCL13 in tumor but was induced to have lower abundance and a greatly impaired immune activation efficacy in GSRCC relative to non-GSRCC.

To probe the susceptibility of GSRCC vs non-GSRCC to ICB, we next evaluated the relative intensity of several established inhibitory checkpoint molecules in CD4<sup>+</sup> and CD8<sup>+</sup> cells at both the RNA and protein levels. In contrast to non-GSRCC, neither CD4<sup>+</sup> nor CD8<sup>+</sup> cells from GSRCC showed up-regulated activation-associated signatures: that is, GSRCC tumors possessed a lower level of ICB target genes, such as HAVCR2, PDCD1, LAG3, CTLA4, and TIGIT, than their non-GSRCC counterparts (Figure 2K and L). Because CD8<sup>+</sup> cells (especially CD8-Tex) are the most well-established targets for ICB, these results suggest a low response rate of GSRCC to ICB.

### T-Cell Responsiveness Is Greatly Impaired in Gastric Signet-Ring Cell Carcinoma

To gain more mechanistic insights, we analyzed matched TCR sequencing from 43,428 T cells and identified numerous T-cell clones of different sizes (Supplementary Tables 4 and 5). Globally, large clones preferred to emerge within fully differentiated subsets, such as Th1-GZMH, Th17, and CD8-Tex (Figure 3A and B), suggesting that they were central responders in TIME. CD4<sup>+</sup> clones responded to tumor antigens substantially in non-GSRCC but were less responsive in GSRCC across all CD4<sup>+</sup> T-cell subsets ( $P = .0078$ ) (Figure 3C and D and Supplementary Figure 3); similarly, expanded CD8<sup>+</sup> clonotypes markedly decreased in GSRCC ( $P = .062$ ) (Figure 3C and D and Supplementary Figure 3). One of the most expanded CD4<sup>+</sup> populations in non-GSRCC was Tfh. Though highly expanded, Tfh clones were small in size, with no more than 5 cells (Figure 3A),

suggesting inferior specificity to tumor antigens. In GSRCC, the expansion of all CD4<sup>+</sup> subsets was notably attenuated, represented by Tfh, Th1, and Treg populations, and CD8-Tex was the predominantly amplified CD8<sup>+</sup> subset, with clones of large size in both non-GSRCC and GSRCC, matching up with its reputation as an antigen-specific population. The entirely restrained expansion of Tn hinted at the possibility of the arrested differentiation of T cells in GSRCC.

For TCR sharing analysis, we detected minimal clonotype sharing among CD4<sup>+</sup> T cells from adjacent noncancerous samples, supporting a strict bifurcation between these phenotypes in the normal condition. It is accessible that Tn amplified and differentiated into effective as well as suppressive cell types to balance the physiologic environment, and obvious clonotypes were shared between 2 Th1 populations or 2 Treg populations, implying their homology. Within non-GSRCC, there were greatly increased TCR overlaps among CD4<sup>+</sup> subsets, and the overlaps were much higher than those in noncancerous samples across different combinations (Figure 3E and F), reflecting a well-mobilized TIME. The increased TCR overlap among Th1, Th17, and Tfh supported the superior responsiveness of these populations that concluded from their amplification capacity (Figure 3E). The increasing dynamic TCR sharing among CD4<sup>+</sup> subsets also showed the heightened plasticity of CD4<sup>+</sup> T cells. The enhanced TCR sharing between 2 Treg subtypes suggested their simultaneous amplification or enhanced phenotype switch in non-GSRCC (Figure 3E). Among CD8<sup>+</sup> populations, Trm acted as a pool of T-cell clones; it amplified and differentiated into diverse subpopulations under stimulation, with respective functions. Broadly, we noted significant overlaps between CD8-Trm and other CD8<sup>+</sup> subsets in the adjacent noncancerous condition, reflecting the key position of CD8-Trm in CD8<sup>+</sup> T-cell differentiation. In non-GSRCC, CD8-Trm shared fewer TCRs with other CD8<sup>+</sup> subsets, ranging from CD8-Tn to terminally exhausted CD8-Tex, concurrent with an exceptional increase in TCR sharing between CD8-Teff and CD8-Tex, being proof of the propensity for exhausted TIME. Additionally, higher TCR overlap between CD8-Tn and CD8-Teff in non-GSRCC vs non-cancerous samples indicates new antigens that have not been recorded in the CD8-Trm pool (Figure 3G).

In contrast to non-GSRCC, the situation of TCR sharing altered markedly in GSRCC (Figure 3E-H). Most visibly, TCR sharing was almost extinguished among CD4<sup>+</sup> subsets, and we

**Figure 2.** T-cell profile in GC revealed by the immune-targeted strategy. (A, B) UMAP plots of subclustered (A) CD4<sup>+</sup> and (B) CD8<sup>+</sup> T cells. (C) Heatmap of T-cell lineage and functional markers used to annotate distinct T-cell subpopulations. (D, E) Box plots showing the relative abundance of (D) CD4<sup>+</sup> and (E) CD8<sup>+</sup> T-cell subpopulations in noncancerous (N) and GC conditions. (F) Box plots showing the relative abundance of CD8-Tex in N/GC (left) and non-GSRCC/GSRCC (right) among the scRNA-seq cohort. (G) Box plots showing the relative abundance of CD8-Tex in N/GC (left) and non-GSRCC/GSRCC (right) among the CyTOF cohort. (H, I) Volcano plot showing differentially expressed genes of CD8-Tex in (H) GC vs N, and (I) GSRCC vs non-GSRCC. Threshold:  $P < .01$  and  $|\log_2 \text{fold change}| > 0.25$ . (J) Box plots showing the differential expression pattern of CXCL13 in CD8-Tex cells from different samples. \* $P < .05$ , \*\* $P < .01$ ; 2-sided unpaired Wilcoxon test. (K, L) Heatmaps of immune checkpoints in CD4 and CD8 T-cell populations from different sample groups (K) in the scRNA-seq cohort and (L) the CyTOF cohort. In D–G, the middle line in the box is the mean, the bottom and top of the box are the first and third quartiles, and the whiskers extend to the 1.5 $\times$  the interquartile range of the lower and the upper quartiles, respectively. Each dot represents 1 sample. \* $P < .05$ , \*\* $P < .01$ , \*\*\* $P < .005$ ; 2-sided paired or unpaired Wilcoxon test. Paired boxes without notation of  $P$  values show no significant difference.

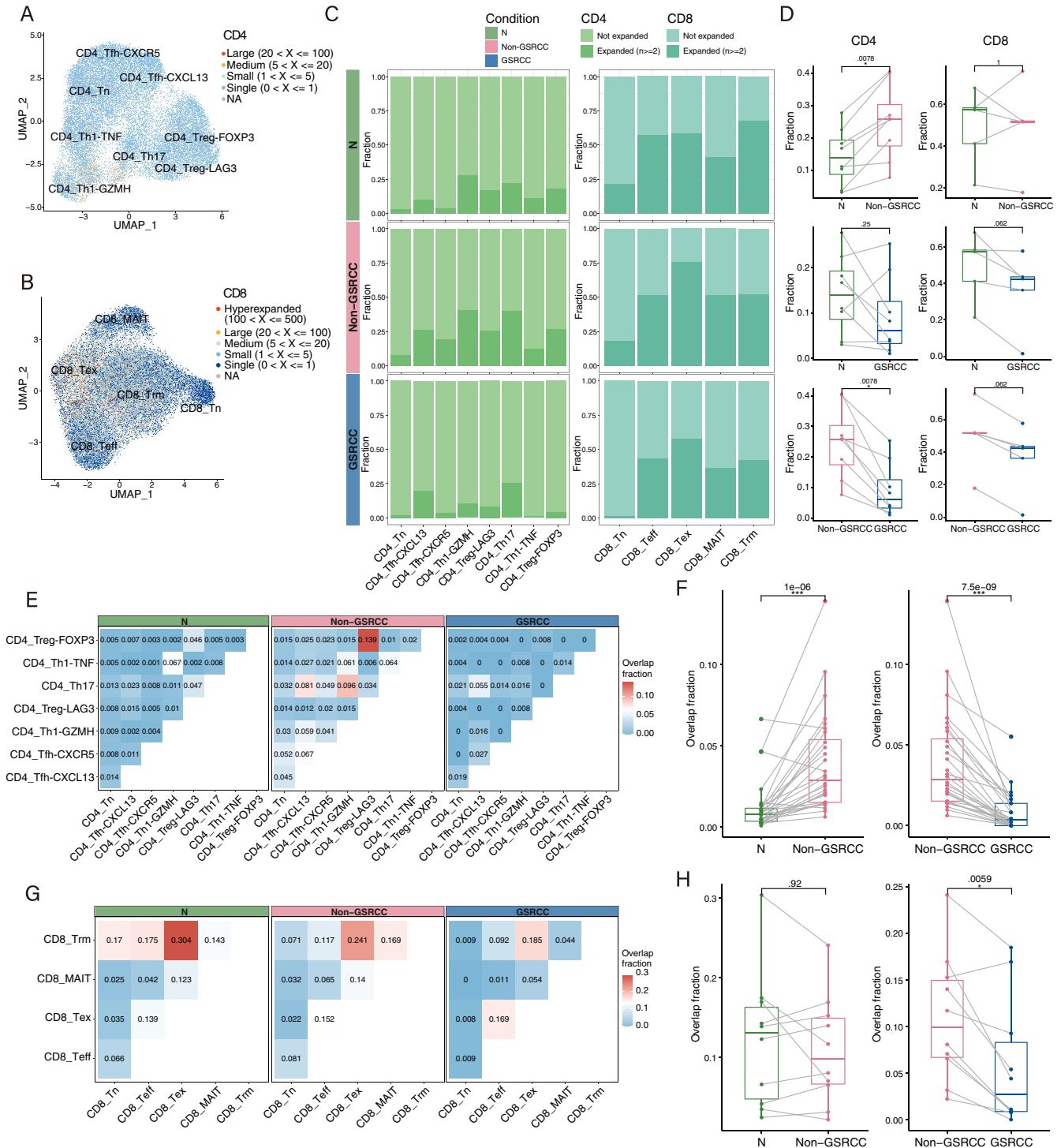


**Figure 3.** Characterization of T-cell responsiveness in GC. (A, B) Visualization of density and clonotype richness across (A) CD4<sup>+</sup> and (B) CD8<sup>+</sup> T-cell clusters, colored according to clone size. (C) Fraction of expanded clonotypes in each CD4<sup>+</sup> (left) and CD8<sup>+</sup> (right) subpopulation from noncancerous (N) (top), non-GSRCC (middle), and GSRCC (bottom). Data are presented as mean values. (D) Box plots showing the fraction difference of expanded clonotypes across different subpopulations. Paired Wilcoxon test. (E, G) TCR sharing of expanded clonotypes across all possible combinations of (E) CD4<sup>+</sup> and (G) CD8<sup>+</sup> T cells in N (left), non-GSRCC (middle), and GSRCC (right). Numbers indicate the ratio of overlapped TCRs for each cluster pair (adjusted  $P < .05$ , 1-sided Fisher's exact test followed by Benjamini-Hochberg correction). (F, H) Box plots showing the ratio difference of overlapped TCRs across all possible combinations of (F) CD4<sup>+</sup> and (H) CD8<sup>+</sup> T cells. Paired Wilcoxon test. NA, not applicable.

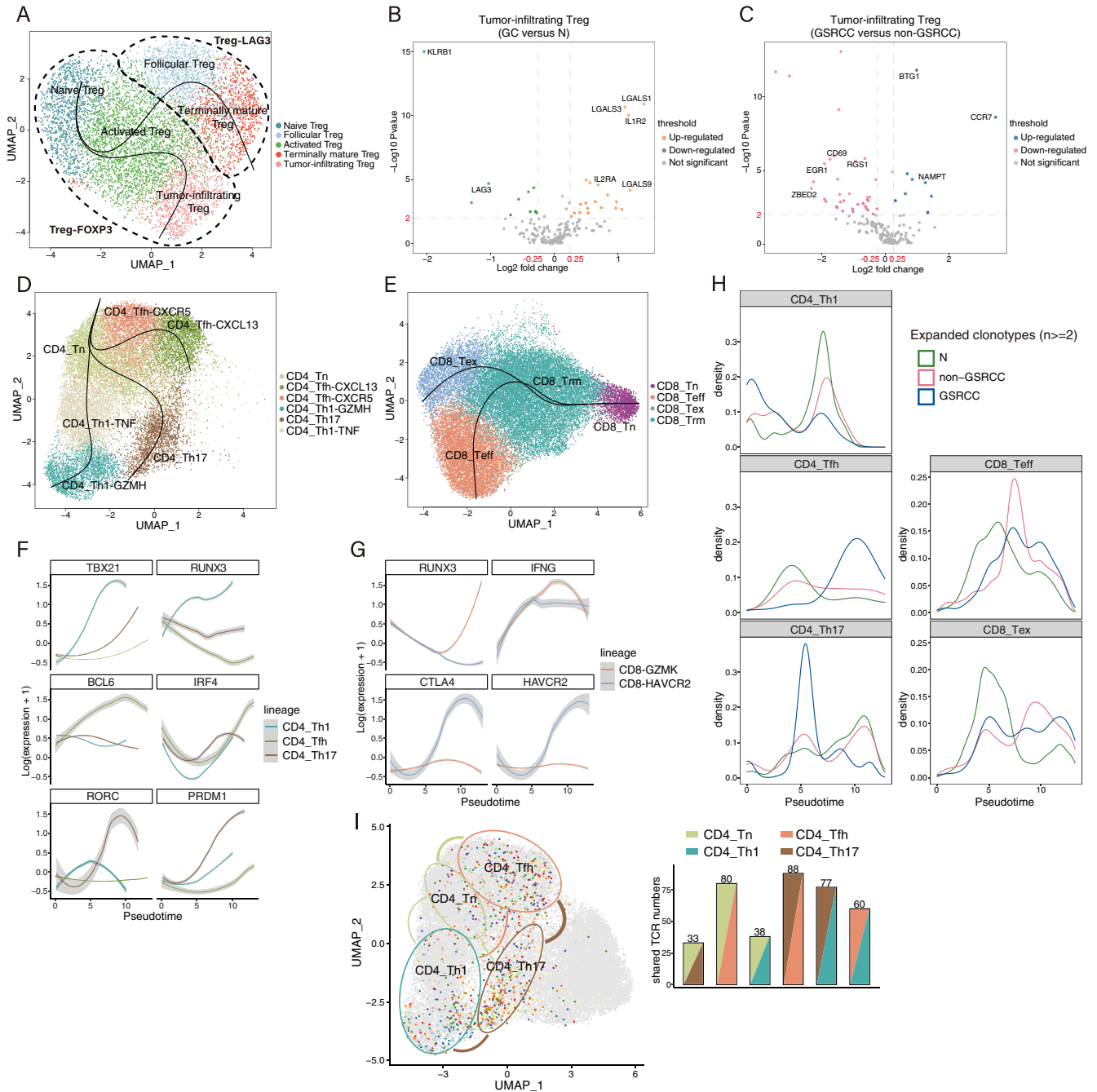


**Figure 4.** Trajectory analysis of T-cell subsets and differentially expressed genes along pseudotime in GC. (A) Pseudotime trajectories for Treg cells based on Slingshot, showing 2 trajectories (terminally mature Treg and tumor-infiltrating Treg cells), color-coded by Treg cell subpopulations. (B, C) Volcano plots presenting differentially expressed genes of tumor-infiltrating Treg in (B) GC vs noncancerous (N) and (C) GSRCC vs non-GSRCC. Threshold:  $P < .01$  and  $|\log_2 \text{fold change}| > 0.25$ . (D) Pseudotime trajectories for canonical CD4<sup>+</sup> T cells based on Slingshot, showing 3 trajectories (Th1, Th17, and Tfh), color-coded by CD4<sup>+</sup> T-cell subpopulations. (E) Pseudotime trajectories for CD8<sup>+</sup> T cells based on Slingshot, showing 2 trajectories (CD8-Teff and CD8-Tex), color-coded for CD8<sup>+</sup> T-cell subpopulations. (F, G) Dynamic expression of (F) lineage-specific markers along the CD4<sup>+</sup> T-cell trajectories and (G) functional markers along the CD8<sup>+</sup> T-cell trajectories. Gray shading in F and G represents the 95% confidence interval for any given pseudotime. (H) Density plots reflecting the relative abundance of expanded T cells along CD4- (left) and CD8-lineages (right). Colored by sample origin (N, non-GSRCC, and GSRCC). (I) Dimplot reflecting the cell state transition of CD4<sup>+</sup> T helper subsets inferred by shared TCRs. Cells sharing TCRs across different CD4<sup>+</sup> T subsets are shown in colors. The thickness of the lines indicates the number of shared TCRs between the 2 connected subsets. The graph in the upper right corner shows the TCR numbers shared by the 2 subsets. The 2 colors in each bar represent the given 2 subsets sharing TCRs.



also observed dramatic attenuation among CD8<sup>+</sup> TCR sharing, except that between CD8-Teff and “negligent” CD8-*Tex*. These findings suggest a differentiation blockade of T cells, especially CD4<sup>+</sup> T cells, in GSRCC TIME. The milieu inside GSRCC seemed to be immune silent because most T cells remained naive or irresponsive to tumor antigens, and this quiescent scenario showed a much more inert TIME in GSRCC.

### Impaired T-Cell Response in Gastric Signet-Ring Cell Carcinoma May Result From Proliferation or Differentiation Blockade

To better understand the transition of T cells during the dynamic biological timeline, we inferred pseudotime trajectories by Slingshot.<sup>22</sup> Considered as noncanonical T subsets with unique differentiation patterns, we processed Treg cells separately and excluded MAIT cells from the CD8<sup>+</sup> pool. Although greatly enriched in non-GSRCC, we identified Treg-FOXP3 primarily as a tumor-induced Treg. This notion was further supported by enhanced suppressive activation (represented by LGALS1, LGALS3, IL2RA) of Treg-FOXP3 in GC<sup>23</sup> (Supplementary Figure 4A). However, the efficacy of tumor-induced Treg-FOXP3 was disparate between GSRCC and non-GSRCC, manifested as a reinforced naive feature (represented by CCR7 and TCF7) and restricted suppressive function (represented by PRDM1, IKZF2, and EGR1) and migration ability (represented by RGS1) in GSRCC<sup>19,24,25</sup> (Supplementary Figure 4B). These findings highlight the internal heterogeneity of Treg cells. We further divided previously annotated Treg-LAG3 into 2 subpopulations: CXCR5-characterized follicular Treg and terminally mature Treg highly expressing effector molecules. Treg-FOXP3 was classified into naive Treg, activated Treg, and tumor-infiltrating Treg, according to their individual profile<sup>26</sup> (Figure 4A and Supplementary Figure 4C and D). There seemed to be polarization among these subsets because follicular Treg and terminally mature Treg are more likely to be universal effector Treg that are enriched in the adjacent noncancerous condition, while naive Treg, activated Treg, and tumor-infiltrating Treg dominate in GC (Supplementary Figure 4E and F), supporting our previous hypothesis. We observed a significant Treg state shift between normal and GC but not between non-GSRCC and GSRCC (Supplementary Figure 4G). Tumor-infiltrating Treg performed differently in non-GSRCC and GSRCC. The differentially expressed genes (DEGs) of tumor-infiltrating Treg cells were almost the same as those of Treg-FOXP3, characterized by enhanced activation in GC but restricted function in GSRCC (Figure 4B and C). Treg-FOXP3 expressed PD-1 was significantly lower in GSRCC than in non-GSRCC (Supplementary Figure 4H). In other words, Treg cells were less responsive in GSRCC and less sensitive to anti-PD-1 treatment.

Canonically, starting with Tn, the differentiation trajectory trifurcated into Th1, Tfh, and Th17 CD4 lineages and bifurcated into Teff and *Tex* CD8 lineages. Located midway along the Th1 and Tfh lineages, respectively, Th1-TNF and Tfh-CXCR5 tally with their annotation as pre-Th1/Tfh. CD8-

Trm appeared to be the distribution center of CD8 lineages (Figure 4D and E). Along pseudotime-based T-cell trajectories, naive markers (ie, CCR7, SELL, and TCF7) decreased, whereas another gene set consisting of inhibitory checkpoints (PDCD1, CTLA4, TIGIT, LAG3, HAVCR2) increased. Specifically, inhibitory signatures emerged at an earlier stage of the CD8-*Tex* lineage than of other lineages. We also detected certain functional DEGs along the trajectories, including some lineage-specific key markers, such as TBX21 and IFNG in the Th-1 lineage; BCL6, IRF4, and CXCL13 in the Tfh lineage; RORC, PRDM1, and IL17F in the Th17 lineage; and activation and cytotoxicity signatures (ie, RUNX3, IFNG, GZMB, TNF) in the CD8-Teff lineage (Figure 4F and G and Supplementary Figure 5B-F).

To discern the dynamic responsiveness of canonical T cells in each condition, we plotted the densities of expanded clones along the pseudotime-based trajectories (Figure 4H). We found impaired Th1 amplification in GC, which was attenuated more vigorously in GSRCC. Tfh showed a delayed augmentation, whereas Th17 was characterized by transiently pronounced augmentation at the middle stage of the trajectory in GSRCC. Considering the frequent TCR sharing between Th17 and Tfh-CXCL13, we reasoned that Th17 mostly converted into Tfh-CXCL13 (Figure 3E). Moreover, we traced identical TCRs along the trajectories and found 88 TCRs shared between Th17 and Tfh cells, more than between Th17 and CD4-Tn (80 shared TCRs). We also observed frequent TCR sharing between Th17 and Th1 (77 shared TCRs) as well as Tfh and Th1 (60 shared TCRs) (Figure 4I). These findings indicate the plasticity of CD4<sup>+</sup> T cells and support the transition between Th17 and Tfh cells. The antitumor response of CD8-Teff was also impaired in GSRCC, whereas CD8-*Tex* kept amplifying, indicating their persistent responses along the process. We next studied DEGs among different conditions, accounting for the discrepancy with clonotype expansion among conditions. On the whole, the cell activation and the function of T cells were mainly dampened in GSRCC, manifested by the down-regulation of activation markers (DUSP1, EGR1, and CD69) and effector signatures (IFNG, GNLY, and NKG7 et al)<sup>27-29</sup> (Supplementary Figure 5G). Strikingly, we found that the inducible costimulatory molecule (ICOS), a proven key factor in regulating CD4<sup>+</sup> T-cell function, immune tolerance, and T-cell-dependent B-cell response,<sup>30</sup> was up-regulated in GSRCC CD4<sup>+</sup> T cells, suggesting its potential as a therapeutic candidate in GSRCC. Differentiation regulators were also obviously suppressed in GSRCC, including FOSB and JUNB, components of the activator protein-1 (AP-1), suggesting the blockade of cell differentiation and loss of T-cell homeostasis in GSRCC.<sup>31,32</sup> Serving as a negative regulator of chemokine receptor signaling in lymphocytes, RGS1 is critical for T-cell migration, especially for Tfh cells, thus further contributing to B-cell behavior.<sup>25,33</sup> RGS1 can also promote T-cell exhaustion by forcing persistent antigen stimulation upon T cells in multiple cancers.<sup>34</sup> Its down-regulation implied an immune-quiescent feature in GSRCC. Even sharply or steadily augmented in GSRCC, the activity and efficiency of Tfh, Th17, CD8-Teff, and CD8-*Tex* were greatly

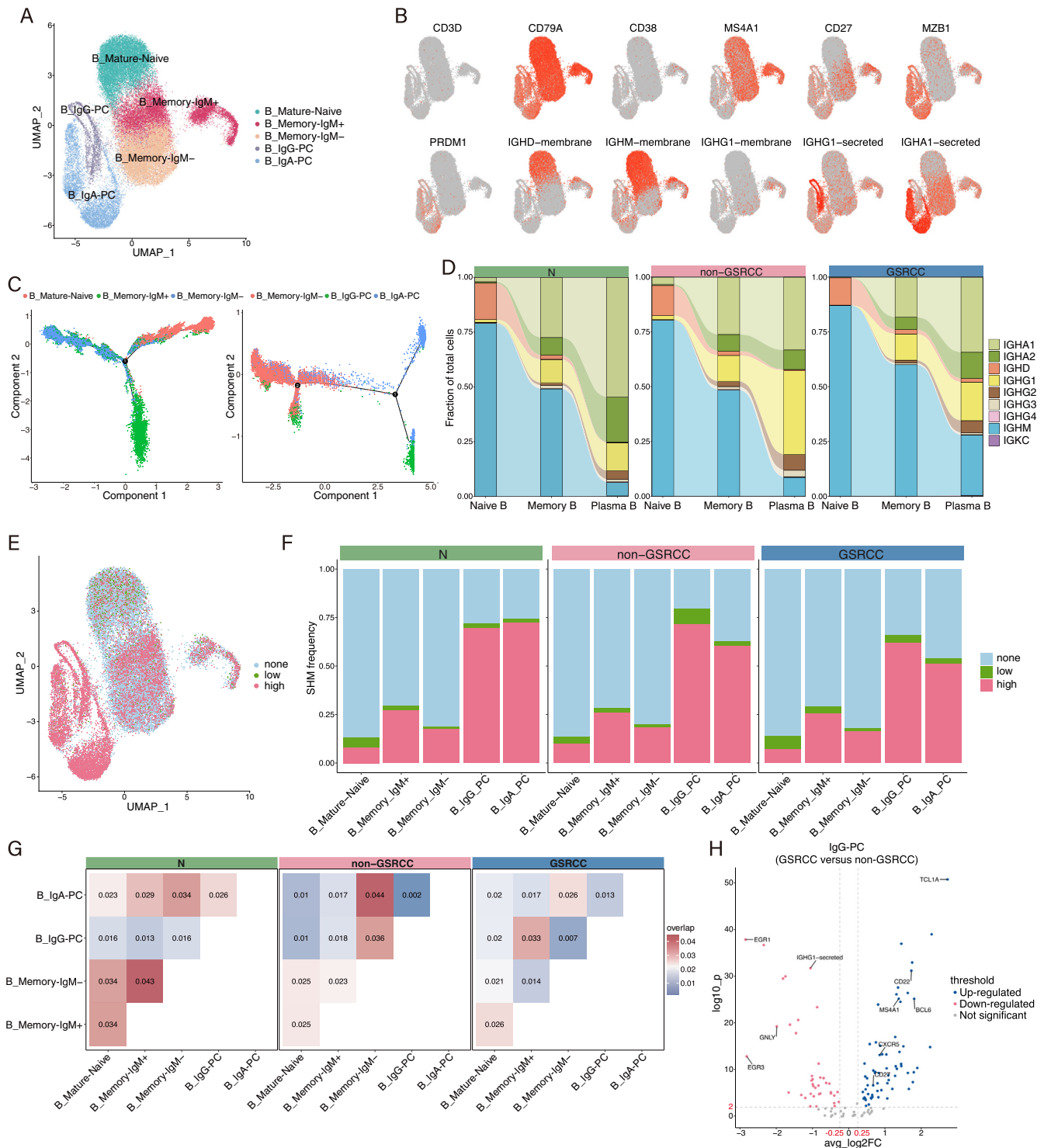


**Figure 5.** Clustering of B cells and BCR analysis in GC. (A) UMAP plot of filtered B cells from 20 GC patients, identifying 5 subpopulations at diverse differentiation stages. (B) UMAP distribution of marker genes representing distinct B-cell types. (C) Pseudotime-based developmental trajectory of B cells inferred by analysis with Monocle 2. (D) Sankey diagram showing the component of diverse immunoglobulins along B-cell development from naive, to memory, to plasma B cells in N (left), non-GSRCC (middle), and GSRCC (right). (E) UMAP plot of B cells with cells color-coded by the SHM level. None, no SHM; low, 0%–3% SHM; high, >3% SHM. (F) Average frequency of BCR SHM levels within each B subset in N (left), non-GSRCC (middle), and GSRCC (right). None, no SHM; low, 0%–3% SHM; high, >3% SHM. (G) BCR sharing of expanded clonotypes across all possible combinations of B cells in N (left), non-GSRCC (middle), and GSRCC (right). Numbers indicate the ratio of overlapped BCR for each cluster pair (adjusted  $P < .05$ , 1-sided Fisher’s exact test followed by Benjamini-Hochberg correction). (H) Volcano plot presenting differentially expressed genes of IgG-PC in GSRCC vs non-GSRCC. Threshold:  $P < .01$  and  $|\log_2 \text{fold change}| > 0.25$ .

attenuated without exception, suggesting their malfunction in GSRCC.

### *B-Cell-Mediated Immune Response Is Dampened in Gastric Signet-Ring Cell Carcinoma*

The mentioned alterations of Tfh, Th17, and CD8-Tex shared a common feature: that their cytokine- and chemokine-producing effects were greatly impaired in GSRCC, especially for CXCL13 (Supplementary Figure 5G), which would subsequently affect B-cell recruitment and/or priming. Therefore, we clustered 44,787 B cells into 5 distinct subtypes (Figure 5A and B). According to their functional genes and pseudotime trajectory analysis, the mature-naïve subset differentiated into either germinal center-memory IgM<sup>+</sup> or IgM<sup>-</sup> branches, accompanied by a decrease in naïve markers (IGHD, IGHM, TCL1A) and an increase in the memory marker, CD27. The memory-IgM<sup>+</sup> cluster is located halfway through the trajectory, suggesting that this population undergoes class-switch recombination into the memory-IgM<sup>-</sup> cluster (Figure 5B and C and Supplementary Figure 6A and B). Under stimulation, memory B cells are expected to further differentiate into antibody-secreting plasma cells (PCs), such as populations highly expressing IGHG or IGHA, respectively, in our data. PRDM1 is required for immunoglobulin secretion and inhibits further immunoglobulin class switching of PCs.<sup>35</sup> We found that PRDM1 was slightly up-regulated along the trajectory, together with another important molecule for immunoglobulin assembly and secretion, MZB1.<sup>36</sup> Concomitantly, MS4A1 (encoding CD20), a gene expressed in all stages of B-cell development except for early pro-B, plasmablasts, and plasma B cells, was down-regulated along the branches. These results indicate the terminal but immature state of IgG-PC and IgA-PC (Figure 5B and C and Supplementary Figure 6A and B).

To better understand B-cell differentiation within TIME, we analyzed BCR-sequencing results by scRepertoire<sup>37</sup> (Supplementary Table 6) and found that expanded clonotypes were largely restricted to PCs that were devoted to humoral immunity, especially the IgG and IgA classes (Supplementary Figure 6D). Generally, fewer expanded B-cell clonotypes were in GSRCC than in non-GSRCC (Supplementary Figure 6E). Different from IgA dominance in adjacent noncancerous mucosa, expanded plasma B cells preferred to be IgG (mainly IgG1) in non-GSRCC. However, both IgA-PC and IgG-PC failed to amplify in GSRCC (Supplementary Figure 6F). Enrichment of IgA in gastrointestinal mucosa is known to maintain the homeostasis of commensals physiologically and protect epithelial cells from attacking.<sup>38</sup> Less abundant than IgA, IgG enhanced mucosal homeostasis by responding to infection, and the major proinflammatory subclass was IgG1.<sup>38</sup> To understand isotype switching along B-cell trajectories, we performed a comparison of immunoglobulin classes with consideration of functional states. Unlike non-GSRCC, a great amount of memory B cells failed to develop into IgG-PC in GSRCC or IgA-PC (Figure 5D), manifesting a poorly responsive landscape.

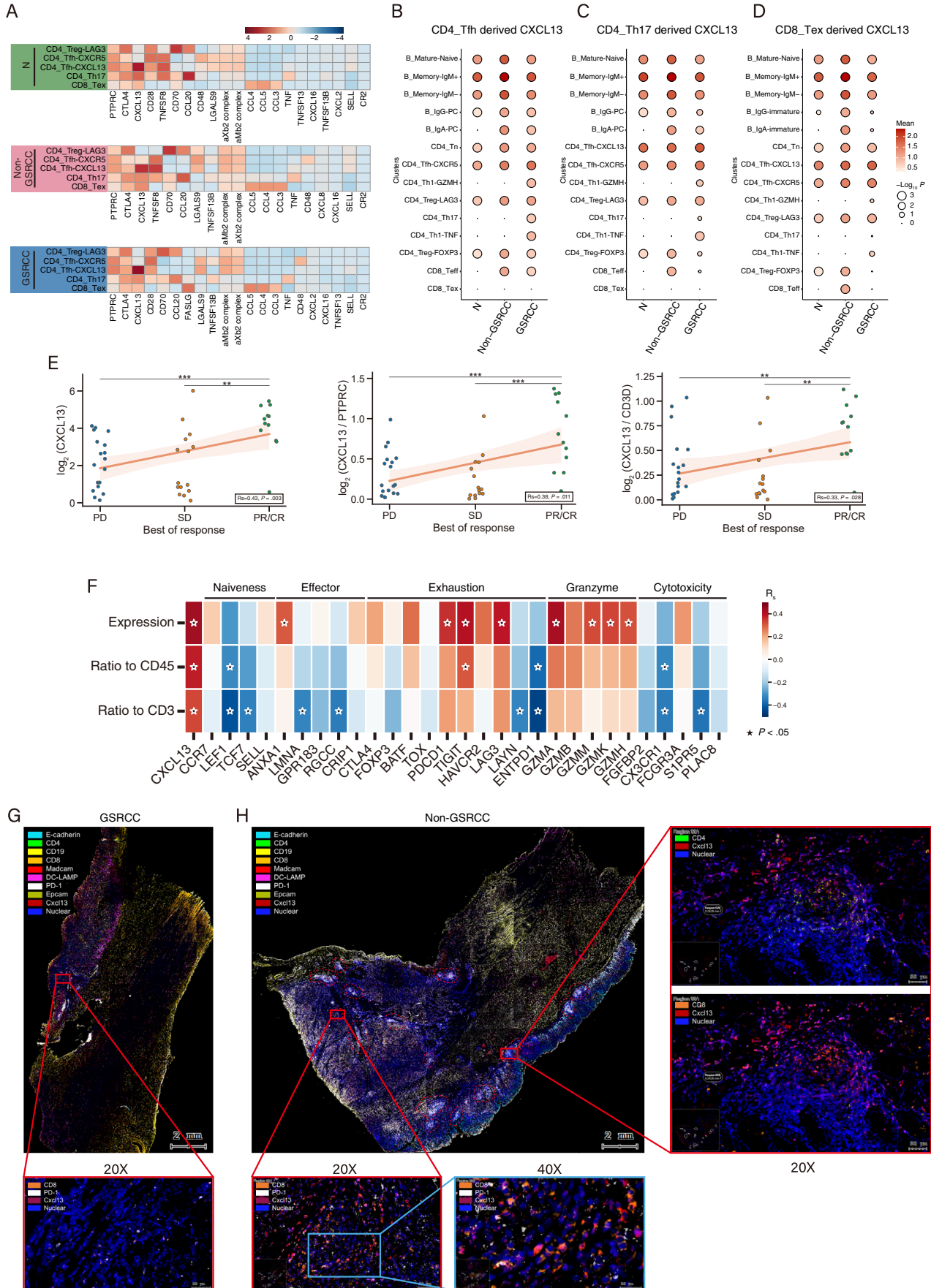
Somatic hypermutation (SHM) is a vital feature of affinity-based selection for B cells. We analyzed BCR-sequencing data and classified B cells into 3 groups: none, low SHM, and high SHM. We found that those in the high SHM group were mainly observed in the BCRs of PCs, followed by the BCRs of memory B cells (Figure 5E and F). B cells with SHM were fewer in GSRCC than in non-GSRCC, implying attenuated antigen-specific priming of B cells in GSRCC (Figure 5F).

According to the BCR sharing profile, IgA-PC normally had the greatest overlap of BCRs because of their dominance and shared the same origin with IgG-PC. However, in non-GSRCC, memory B cells more frequently polarized into IgG-PC, showing significantly lowered homology between IgA-PC and IgG-PC (Figure 5G). IgG seems to respond to antigens that are not only pathogen related but tumor associated as well. We noted remarkable BCR overlap between IgM<sup>+</sup> memory B cells and IgG-PC in GSRCC, unlike the sharing between IgM<sup>-</sup> memory B cells and IgG-PC in non-GSRCC, reflecting the abnormal origin of IgG that led to malfunction in GSRCC (Figure 5H). Verified by DEGs, IgG-PC in GSRCC were premature, with more signatures of the early stage of development (presented by TCL1A, CD22, MS4A1, CXCR5) but lowered activation- and function-related markers (eg, EGR1, EGR3, GNLY, IGHG1 secreted) (Figure 5H). Thus, the impaired antitumor effect of IgG-PC may also contribute to the worse prognosis of GSRCC patients.<sup>39</sup>

### *CXCL13 Is a Central Mediator for the Immune Response of the Gastric Cancer Tumor Immune Microenvironment*

Our results show the poor infiltration of both T and B lymphocytes in GSRCC (Supplementary Figure 6G). To understand how these components jointly create a physiologic or pathologic gastric environment, we characterized extensive interactions among adaptive immunocytes by CellPhoneDB analysis.<sup>40</sup> Both the number and the strength of inferred interactions were elevated in GC, especially in non-GSRCC (Supplementary Figure 7A). Among inferred signaling, the increased interactions in GC were mainly derived from Tfh (CD4-CXCL13 and CD4-CXCR5), imposed on almost all kinds of cells. In non-GSRCC, Treg-LAG3, Th17, and CD8-Tex also contributed to enhanced cell communication (Supplementary Figure 7B and C). A common product that was heavily secreted by these populations turned out to be CXCL13, in both non-GSRCC and GSRCC (Figure 6A), and the expression of CXCL13 in these T subsets was greatly impaired in GSRCC (Supplementary Figure 7D). As the well-accepted receptor of CXCL13, CXCR5 owned the leading contribution to CXCL13 signaling. We then analyzed specific interactions mediated by CXCL13-CXCR5 signaling according to different CXCL13 origins. CXCL13-mediated interactions derived from Tfh, Th17, and CD8-Tex were primarily enhanced in GC. In GSRCC, Tfh showed significantly strengthened regulation on Th1 and Th17, whereas Th17 and CD8-Tex exhibited inferior regulation on PC, Treg-FOXP3, and CD8-Teff (Figure 6B–D). In the absence of cytotoxic CD8-Teff and appropriate humoral immune response, enhanced







recruitment of Th1 and Th17 would harm tumor control by promoting proinflammatory conditions excessively.<sup>41</sup> This finding suggests a vital role of CXCL13 in determining TIME heterogeneity, and the contribution of CD8-Tex in CXCL13 production is indispensable.

### CXCL13 Expression Predicts Immune Checkpoint Blockade Response in Gastric Cancer Patients

We then hypothesized that the baseline activity of CXCL13 within a tumor may inform the efficacy of ICB treatment. To test this hypothesis, we analyzed a published bulk RNA-seq dataset of pre-ICB-treatment tumor samples from GC patients<sup>42</sup> and found a strong positive association between CXCL13 expression and therapeutic response even when corrected for CD45 and CD3 expressions, which were used as proxies of overall immune infiltration or T-cell abundance, respectively (Figure 6E). Surprisingly, CXCL13 was the only gene that showed consistently significant correlations with the response among a wide panel of canonical T-cell state markers (Figure 6F).

The aforementioned findings reminded us of tertiary lymphoid structures (TLSs). TLSs provide an appropriate niche for cell communications, as well as for the initiation and/or maintenance of the T- and B-cell responses, leading to a magnified antitumor immune response and favorable outcomes.<sup>43</sup> CXCL13 was recognized as a typical marker of TLSs and participates throughout TLS organizations. The existence of TLSs has been proposed as indispensable for CXCL13<sup>+</sup>CD4<sup>+</sup> and CXCL13<sup>+</sup>CD8<sup>+</sup> T cells to achieve clinical benefit.<sup>44</sup> Therefore, it is likely that CXCL13 induces TIME heterogeneity by interfering with the formation of TLSs in GSRCC. To test this hypothesis, we analyzed H&E-stained slides of another cohort of GC patients (non-GSRCC, n = 68; GSRCC, n = 26) (Supplementary Table 7) and, indeed, observed the lower frequency of TLSs within GSRCC than within non-GSRCC tissues (Supplementary Figure 7F and G). We further characterized cancer tissue sections for multiplex immunohistochemistry staining to reveal the spatial relationship of this coordinator. Primary screening with a simple staining panel (CD8, CD19, and CXCL13) showed that abundant T-/B-cell aggregations were less likely to be found in GSRCC than in non-GSRCC (Supplementary Figure 7H). Considering the heterogeneity of GSRCC tissues and the strict definition of TLSs, we used an expanded staining panel

with up to 9 specific markers and nuclear staining on representative GSRCC and non-GSRCC samples. Indeed, we found barely visible TLSs in GSRCC but widespread well-organized TLSs in non-GSRCC (Figure 6G and H). Substantial CXCL13<sup>+</sup>CD4<sup>+</sup> and CXCL13<sup>+</sup>CD8<sup>+</sup> T cells were found within TLSs (Figure 6H). Because PD-1 expression was generally low, the coexpression of PD-1 and CXCL13 could be detected on CD8<sup>+</sup> T cells, indicating the CXCL13-expressing ability of CD8-Tex cells, which was weak in GSRCC (Figure 6G and H).

## Discussion

Focusing on advanced GC, our study provides a comparative analysis of TIME between GSRCC and non-GSRCC and has 2 important features. First, through the joint single-cell transcriptomic and proteomic analysis of GC TIME, our findings at the RNA level can be directly validated at the protein level, which greatly increases the credibility. Second, because of our immune-targeted profiling strategy, the amount of tumor-infiltrating immunocytes included is unprecedented, which allows us to characterize the TIME in great detail. We show that TIME heterogeneity derived from advanced GSRCC is distinct from non-GSRCC and that effector CD4<sup>+</sup> and CD8<sup>+</sup> T cells are generally restrained in GSRCC, mainly by limiting cell activation as well as expansion. The enhanced conversion between Th17 and Tfh suggests disturbed CD4<sup>+</sup> T-cell development in GSRCC. In parallel, we observe that B cells could also not develop into effective plasma B cells in GSRCC.

Our study highlights the critical role of CXCL13 in shaping the TIME of advanced GSRCC. Though less cytotoxic, CD8-Tex is induced to acquire the ability to produce chemoattracting CXCL13. More recently, CXCL13 has been identified as a unique marker for tumor antigen-specific CD4<sup>+</sup> and CD8<sup>+</sup> T cells, including CD8-Tex.<sup>44,45</sup> The re-educated CXCL13<sup>+</sup> CD8-Tex is proposed to recruit other immunocytes, thereby facilitating the initiation of TLS formation in individuals with tumors. However, CD8-Tex in GSRCC could not achieve this progression and became incompetent. Thus, the down-regulation of this CXCL13-mediated regulatory effect in CD8-Tex would contribute to dismal outcomes in GSRCC patients.

Various lines of evidence refer to the orchestrated alteration of TIME in GSRCC, leading us to the concept of TLSs. CXCL13 performs as a crucial element because of its

**Figure 6.** Differential regulatory effects of CXCL13 on GC TIME and ICB response. (A) Heatmap showing ligands expressed by the sources (Treg-LAG3, Tfh-CXCL13, Tfh-CXCR5, Th17, CD8-Tex) of differential secreted interactions in noncancerous (N) (top), non-GSRCC (middle), and GSRCC (bottom). (B–D) Dot plots showing the significance ( $-\log_{10} P$  value) and strength (mean value) of specific interactions mediated by CXCL13-CXCR5 between (B) Tfh, (C) Th17, or (D) CD8-Tex and other adaptive immunocytes by comparing N, non-GSRCC, and GSRCC. (E) Scatter plots showing the association between patient response to ICB treatment and CXCL13 expression (left), CXCL13-PTPRC expression ratio (middle), and CXCL13-CD3D expression ratio (right). \*\* $P < .01$ , \*\*\* $P < .001$ ; Spearman rank correlation. (F) Heatmap showing the same correlations as at the top for all surveyed marker genes. The stars indicate statistical significance. (G, H) Multiplex immunohistochemistry using tyramide signal amplification-based detection methods and multispectral imaging. Representative GC sections of (G) GSRCC and (H) non-GSRCC were stained with E-cadherin (cyan), CD4 (green), CD19 (yellow), CD8 (orange), Madcam (red), DC-LAMP (magenta), PD-1 (white), Epcam (olive), CXCL13 (maroon), and nuclear (blue). Scale bar, 2 mm in whole scenes; scale bar, 50  $\mu\text{m}$  in 20 $\times$  view; scale bar, 20  $\mu\text{m}$  in 40 $\times$  view. CR, complete response; PD, progressive disease; PR, partial response;  $R_s$ , Spearman correlation coefficient; SD, stable disease.

full participation throughout the TLS organization, thus highlighting the pivotal role of CXCL13-producing cells, such as Tfh, Th17, and CD8-Tex presented in our results. Stimulated by GC antigens, the modulatory effect of all these subsets was upgraded in a CXCL13-dependent manner. As an exception to this, enhanced interaction derived from Treg-LAG3 in non-GSRCC was mediated by LGALS9 to avoid the excessive immune response. It is well established that Tfh functions effectively in cell recruitment and activation and performs as an indispensable and sufficient inducer of TLS formation in tumor sites.<sup>46</sup>

Finally, our findings underline the importance of CXCL13-producing CD8-Tex in promoting antitumor response. CD8-Tex is a better indicator for recruiting tumor-reactive immunocytes because of its higher specificity to tumor antigens than Tfh. Specifically, CD8-Tex-derived CXCL13 was unlikely to interact with immune suppressive tumor-associated Treg-FOXP3, partly accounting for the reduction of Treg-FOXP3 infiltrated in GSRCC. We thus postulated that CXCL13 secreting CD8-Tex was the preferable target in this therapeutic strategy. Impaired CD8-Tex-derived modulation in GSRCC was very likely to be responsible for the inadequate immune response in GSRCC. Thus, for non-GSRCC patients, it may be feasible for them to take conventional treatment, including chemotherapy and/or ICB therapy, whereas for GSRCC patients, it may be crucial to improve the CXCL13-producing ability of CD8-Tex cells to reverse the refractory condition. In future, we will use inflammation-induced GC mouse models to investigate the pivotal signals that regulate CXCL13 production specifically in CD8-Tex cells.

## Supplementary Material

Note: To access the supplementary material accompanying this article, visit the online version of *Gastroenterology* at [www.gastrojournal.org](http://www.gastrojournal.org), and at <https://doi.org/10.1053/j.gastro.2023.03.008>.

## References

- Sung H, Ferlay J, Siegel RL, et al. Global cancer statistics 2020: GLOBOCAN estimates of incidence and mortality worldwide for 36 cancers in 185 countries. *CA Cancer J Clin* 2021;71:209–249.
- Chia NY, Tan P. Molecular classification of gastric cancer. *Ann Oncol* 2016;27:763–769.
- Lauren P. The two histological main types of gastric carcinoma: diffuse and so-called intestinal-type carcinoma. An attempt at a histo-clinical classification. *Acta Pathol Microbiol Scand* 1965;64:31–49.
- Piessen G, Messenger M, Leteurtre E, et al. Signet ring cell histology is an independent predictor of poor prognosis in gastric adenocarcinoma regardless of tumoral clinical presentation. *Ann Surg* 2009;250:878–887.
- Smyth EC, Nilsson M, Grabsch HI, et al. Gastric cancer. *Lancet* 2020;396:635–648.
- Kang YK, Boku N, Satoh T, et al. Nivolumab in patients with advanced gastric or gastro-oesophageal junction cancer refractory to, or intolerant of, at least two previous chemotherapy regimens (ONO-4538-12, ATTRACTION-2): a randomised, double-blind, placebo-controlled, phase 3 trial. *Lancet* 2017;390:2461–2471.
- Fuchs CS, Doi T, Jang RW, et al. Safety and efficacy of pembrolizumab monotherapy in patients with previously treated advanced gastric and gastroesophageal junction cancer: phase 2 clinical KEYNOTE-059 trial. *JAMA Oncol* 2018;4:e180013.
- Shitara K, Ozguroglu M, Bang YJ, et al. Pembrolizumab versus paclitaxel for previously treated, advanced gastric or gastro-oesophageal junction cancer (KEYNOTE-061): a randomised, open-label, controlled, phase 3 trial. *Lancet* 2018;392:123–133.
- Zhang M, Hu S, Min M, et al. Dissecting transcriptional heterogeneity in primary gastric adenocarcinoma by single cell RNA sequencing. *Gut* 2021;70:464–475.
- Wang R, Dang M, Harada K, et al. Single-cell dissection of intratumoral heterogeneity and lineage diversity in metastatic gastric adenocarcinoma. *Nat Med* 2021;27:141–151.
- Lei X, Lei Y, Li JK, et al. Immune cells within the tumor microenvironment: Biological functions and roles in cancer immunotherapy. *Cancer Lett* 2020;470:126–133.
- Kashima Y, Togashi Y, Fukuoka S, et al. Potentiality of multiple modalities for single-cell analyses to evaluate the tumor microenvironment in clinical specimens. *Sci Rep* 2021;11:341.
- Sathe A, Grimes SM, Lau BT, et al. Single-cell genomic characterization reveals the cellular reprogramming of the gastric tumor microenvironment. *Clin Cancer Res* 2020;26:2640–2653.
- Lee HO, Hong Y, Etioglu HE, et al. Lineage-dependent gene expression programs influence the immune landscape of colorectal cancer. *Nat Genet* 2020;52:594–603.
- Jeong HY, Ham IH, Lee SH, et al. Spatially distinct reprogramming of the tumor microenvironment based on tumor invasion in diffuse-type gastric cancers. *Clin Cancer Res* 2021;27:6529–6542.
- Korsunsky I, Millard N, Fan J, et al. Fast, sensitive and accurate integration of single-cell data with Harmony. *Nat Methods* 2019;16:1289–1296.
- Zheng L, Qin S, Si W, et al. Pan-cancer single-cell landscape of tumor-infiltrating T cells. *Science* 2021;374:abe6474.
- Adeegbe DO, Nishikawa H. Natural and induced T regulatory cells in cancer. *Front Immunol* 2013;4:190.
- Kim HJ, Barnitz RA, Kreslavsky T, et al. Stable inhibitory activity of regulatory T cells requires the transcription factor Helios. *Science* 2015;350:334–339.
- Wherry EJ, Kurachi M. Molecular and cellular insights into T cell exhaustion. *Nat Rev Immunol* 2015;15:486–499.
- Castillo-Gonzalez R, Cibrian D, Fernandez-Gallego N, et al. Galectin-1 expression in CD8<sup>+</sup> T lymphocytes

- controls inflammation in contact hypersensitivity. *J Invest Dermatol* 2021;141:1522–1532.
22. Street K, Risso D, Fletcher RB, et al. Slingshot: cell lineage and pseudotime inference for single-cell transcriptomics. *BMC Genomics* 2018;19:477.
  23. Hsu DK, Chen HY, Liu FT. Galectin-3 regulates T-cell functions. *Immunol Rev* 2009;230:114–127.
  24. Cretney E, Leung PS, Trezise S, et al. Characterization of Blimp-1 function in effector regulatory T cells. *J Autoimmun* 2018;91:73–82.
  25. Gibbons DL, Abeler-Dorner L, Raine T, et al. Cutting edge: regulator of G protein signaling-1 selectively regulates gut T cell trafficking and colitic potential. *J Immunol* 2011;187:2067–2071.
  26. Wing JB, Tanaka A, Sakaguchi S. Human FOXP3<sup>+</sup> regulatory T cell heterogeneity and function in autoimmunity and cancer. *Immunity* 2019;50:302–316.
  27. Liu Y, Shepherd EG, Nelin LD. MAPK phosphatases—regulating the immune response. *Nat Rev Immunol* 2007;7:202–212.
  28. Singh A, Svaren J, Grayson J, et al. CD8 T cell responses to lymphocytic choriomeningitis virus in early growth response gene 1-deficient mice. *J Immunol* 2004;173:3855–3862.
  29. Cibrian D, Sanchez-Madrid F. CD69: from activation marker to metabolic gatekeeper. *Eur J Immunol* 2017;47:946–953.
  30. Dong C, Juedes AE, Temann UA, et al. ICOS costimulatory receptor is essential for T-cell activation and function. *Nature* 2001;409:97–101.
  31. Baumann S, Hess J, Eichhorst ST, et al. An unexpected role for FosB in activation-induced cell death of T cells. *Oncogene* 2003;22:1333–1339.
  32. Katagiri T, Kameda H, Nakano H, et al. Regulation of T cell differentiation by the AP-1 transcription factor JunB. *Immunol Med* 2021;44:197–203.
  33. Caballero-Franco C, Kissler S. The autoimmunity-associated gene *RGS1* affects the frequency of T follicular helper cells. *Genes Immun* 2016;17:228–238.
  34. **Bai Y, Hu M, Chen Z, et al.** Single-cell transcriptome analysis reveals *RGS1* as a new marker and promoting factor for T-cell exhaustion in multiple cancers. *Front Immunol* 2021;12:767070.
  35. **Shaffer AL, Lin KI, Kuo TC, et al.** Blimp-1 orchestrates plasma cell differentiation by extinguishing the mature B cell gene expression program. *Immunity* 2002;17:51–62.
  36. Flach H, Rosenbaum M, Duchniewicz M, et al. Mzb1 protein regulates calcium homeostasis, antibody secretion, and integrin activation in innate-like B cells. *Immunity* 2010;33:723–735.
  37. Borchering N, Bormann NL, Kraus G. scRepertoire: an R-based toolkit for single-cell immune receptor analysis. *F1000Res* 2020;9:47.
  38. **Chen K, Magri G, Grasset EK, et al.** Rethinking mucosal antibody responses: IgM, IgG and IgD join IgA. *Nat Rev Immunol* 2020;20:427–441.
  39. **Hu X, Zhang J, Wang J, et al.** Landscape of B cell immunity and related immune evasion in human cancers. *Nat Genet* 2019;51:560–567.
  40. Efremova M, Vento-Tormo M, Teichmann SA, et al. CellPhoneDB: inferring cell-cell communication from combined expression of multi-subunit ligand-receptor complexes. *Nat Protoc* 2020;15:1484–1506.
  41. Pelletier N, McHeyzer-Williams LJ, Wong KA, et al. Plasma cells negatively regulate the follicular helper T cell program. *Nat Immunol* 2010;11:1110–1118.
  42. **Kim ST, Cristescu R, Bass AJ, et al.** Comprehensive molecular characterization of clinical responses to PD-1 inhibition in metastatic gastric cancer. *Nat Med* 2018;24:1449–1458.
  43. Sautes-Fridman C, Petitprez F, Calderaro J, et al. Tertiary lymphoid structures in the era of cancer immunotherapy. *Nat Rev Cancer* 2019;19:307–325.
  44. **He J, Xiong X, Yang H, et al.** Defined tumor antigen-specific T cells potentiate personalized TCR-T cell therapy and prediction of immunotherapy response. *Cell Res* 2022;32:530–542.
  45. Thommen DS, Koelzer VH, Herzig P, et al. A transcriptionally and functionally distinct PD-1<sup>+</sup> CD8<sup>+</sup> T cell pool with predictive potential in non-small-cell lung cancer treated with PD-1 blockade. *Nat Med* 2018;24:994–1004.
  46. Overacre-Delgoffe AE, Bumgarner HJ, Cillo AR, et al. Microbiota-specific T follicular helper cells drive tertiary lymphoid structures and anti-tumor immunity against colorectal cancer. *Immunity* 2021;54:2812–2824.

Author names in bold designate shared co-first authorship.

Received September 20, 2022. Accepted March 1, 2023.

#### Correspondence

The authors thank Kamalika Mojumdar for editorial assistance; and YiSong Xu and Hongduo Sun from BD Biosciences/Multiomics for their technical support in scRNA-seq process. The authors also thank TissueGnostics Asia Pacific limited (Beijing, China) for their technical support for multiplexed immunofluorescence staining, image scanning and analysis, and the help of Xiaojing Liu, the technical engineer.

Address correspondence to: Jian Chen, MD, PhD, 88 Jiefang Road, Shangcheng District, Hangzhou, China, 310009. e-mail: [zrchenjian@zju.edu.cn](mailto:zrchenjian@zju.edu.cn); or Lie Wang, PhD, 866 Yuhangtang Road, Hangzhou, China, 310058. e-mail: [wanglie@zju.edu.cn](mailto:wanglie@zju.edu.cn); or Han Liang, PhD, 1400 Pressler Street, Houston, Texas 77030. e-mail: [hliang1@mdanderson.org](mailto:hliang1@mdanderson.org).

#### Acknowledgments

The authors thank Kamalika Mojumdar for editorial assistance; and YiSong Xu and Hongduo Sun from BD Biosciences/Multiomics for their technical support in scRNA-seq process. The authors also thank TissueGnostics Asia Pacific limited (Beijing, China) for their technical support for multiplexed immunofluorescence staining, image scanning and analysis, and the help of Xiaojing Liu, the technical engineer.

#### CRedit Authorship Contributions

Jing Chen, MD, PhD (Investigation: Lead; Writing – original draft: Lead).  
 Kuai Liu, M.M. (Investigation: Lead; Writing – original draft: Lead).  
 Yikai Luo, BS (Investigation: Lead; Writing – original draft: Lead).  
 Muxing Kang, MD, PhD (Investigation: Supporting).  
 Jun Wang, MD, PhD (Investigation: Supporting).  
 Guofeng Chen, MD (Investigation: Supporting).  
 Jia Qi, MD (Investigation: Supporting).  
 Wenxuan Wu, MD (Investigation: Supporting).  
 Beidi Wang, MD (Investigation: Supporting).  
 Yaxuan Han, MD (Investigation: Supporting).  
 Le Shi, MD (Investigation: Supporting).  
 Kefan Wang, MD (Investigation: Supporting).  
 Xiaying Han, MD (Investigation: Supporting).  
 Xiaojing Ma, MD (Investigation: Supporting).  
 Wei Liu, PhD (Investigation: Supporting).  
 Yuan Ding, MD, PhD (Investigation: Supporting).  
 Liangjing Wang, MD (Investigation: Supporting).  
 Han Liang, PhD (Conceptualization: Lead; Investigation: Lead; Project administration: Lead; Writing – review & editing: Lead).  
 Lie Wang, PhD (Conceptualization: Lead; Investigation: Lead; Writing – review & editing: Lead).  
 Jian Chen, MD, PhD (Conceptualization: Lead; Funding acquisition: Lead; Investigation: Lead; Writing – review & editing: Lead).

**Conflicts of interest**

This author discloses the following: Han Liang is a shareholder and scientific advisor of Precision Scientific Ltd. The remaining authors disclose no conflicts.

**Funding**

This study was supported by grants from the Zhejiang Provincial Key Project of Research and Development (No. 2019C03043, funded by Science Technology Department of Zhejiang Province, China), the National Natural Science Foundation of China (Nos. 32030035, 31870874, 32000623, and 32100693), the Zhejiang Provincial Natural Science Foundation of China (No.

LZ21C080001), Science and Technology Innovation 2030–Major Project (2021ZD0200405), Preresearch Projects of Innovation Center of Yangtze River Delta, Zhejiang University (No. 2022ZY008), and the Barnhart Family Distinguished Professorship in Targeted Therapies from the University of Texas MD Anderson Cancer Center.

**Data Availability**

The processed data in this study have been deposited in Gene Expression Omnibus under the accession number GSE212212, as well as in the Genome Sequence Archive for Human under the accession number HRA002796.